Inverse designed WS_2 planar chiral metasurface with geometric phase

OPEN ACCESS
IOP Publishing
Journal of Optics
J. Opt. **26** (2024) 085101 (9pp)
https://doi.org/10.1088/2040-8986/ad53df

Inverse designed WS_2 planar chiral metasurface with geometric phase

Jaegang Jo[1], Sangbin Lee[2], Munseong Bae[1], Damian Nelson[3], Kenneth B Crozier[3,4,5], Nanfang Yu[6], Haejun Chung[1,2,*] and Sejeong Kim[4,*]

[1] Department of Electronic Engineering, Hanyang University, Seoul 04763, Republic of Korea
[2] Artificial Intelligence Semiconductor Engineering, Hanyang University, Seoul 04763, Republic of Korea
[3] School of Physics, University of Melbourne, Melbourne, Victoria 3010, Australia
[4] Department of Electrical Engineering, Faculty of Engineering and Information Technology, University of Melbourne, Melbourne, Victoria 3010, Australia
[5] Australian Research Council (ARC) Centre of Excellence for Transformative Meta-Optical Systems (TMOS), University of Melbourne, Melbourne, Victoria 3010, Australia
[6] Department of Applied Physics and Applied Mathematics, Columbia University, New York, NY 10027, United States of America

E-mail: haejun@hanyang.ac.kr and sejeong.kim@unimelb.edu.au

Received 2 February 2024, revised 23 May 2024
Accepted for publication 4 June 2024
Published 19 June 2024

Abstract

Increasing attention is being paid to chiral metasurfaces due to their ability to selectively manipulate right-hand circularly polarized light or left-hand circularly polarized light. The thin nature of metasurfaces, however, poses a challenge in creating a device with effective phase modulation. Plasmonic chiral metasurfaces have attempted to address this issue by increasing light–matter interaction, but they suffer from metallic loss. Dielectric metasurfaces made from high-index materials enable phase modulation while being thin. Very few materials, however, have high refractive index and low loss at visible wavelengths. Recently, some 2D materials have been shown to exhibit high refractive index and low loss in the visible wavelengths, positioning them as promising platforms for meta-optics. This study introduces and details a planar chiral metasurface with a geometric phase composed of WS_2 meta-units. By employing adjoint optimization techniques, we achieved broadband circular dichroism (>0.5 in the wavelength range of 653–796 nm) and a high extinction ratio (19.6 dB at $\lambda = 675$ nm).

Keywords: chiral metasurface, transition metal dichalcogenide (TMD), WS_2, dielectric metasurface, geometric phase, inverse design, adjoint optimization

1. Introduction

Metasurfaces, which consist of ultrathin metallic or dielectric nanostructures with dimensions smaller than the wavelength of light, have gained attention for their ability to manipulate optical phase, amplitude, and polarization over the wavefront with subwavelength resolution [1–5]. They have found numerous applications, including ultra-thin meta-lenses [6–8], holograms [1, 9–13], and optical vortex beam generators [3, 14–17]. Geometric-phase-based metasurfaces utilizing the Pancharatnam–Berry phase have attracted considerable attention due to their broadband and efficient manipulation of the optical phase [2, 4, 6, 18–20]. The geometric phase is achieved by rotating a unit cell or meta-unit of metasurfaces, which converts circularly polarized incident light into transmitted light wave with the opposite handedness. This spin-switching capability enables a range of applications, including chiral-sensitive imaging [21, 22] and display [9, 12, 23, 24], and optical spin–orbit coupling [16, 25]. However,

* Authors to whom any correspondence should be addressed.

conventional geometric-phase-based metasurfaces, which feature in-plane mirror symmetry in their meta-units, are limited in their capability to independently modulate the two circularly polarized states. To address this issue, chiral metasurfaces have been proposed, with their broken in-plane mirror symmetry allowing independent control of the two circular polarization states of the transmitted light [26–33]. Such metasurfaces can be designed, for example, to maximize the transmission of circularly polarized light with a particular handedness while simultaneously blocking that with the opposite handedness.

Chiral metasurfaces can be designed with two types of materials: metals and dielectrics. While plasmonic chiral metasurfaces have demonstrated significant circular dichroism (CD) in the visible range, they suffer from significant ohmic losses [27, 30, 34, 35]. Chiral metasurfaces made of dielectric material display negligible absorption; however, they often exhibit low CD or require considerable thickness to attain sufficient light-matter interactions for effective phase manipulation [26, 28, 29, 36]. Therefore, it is challenging to create a thin, planar device that shows both high CD and low absorption in the visible.

In order to achieve a high level of CD in the visible range, we propose a planar chiral metasurface based on WS_2. WS_2 belongs to the family of transition metal dichalcogenides (TMDs) and has attracted considerable attention in the nanophotonics and metasurfaces community due to its high refractive index and strong optical anisotropy [37–41]. The high refractive index of WS_2, larger than 4 in the visible range, allows for a strong interaction between light and the material [42], which increases the polarization conversion efficiency and therefore decreases the required material thickness. Furthermore, the multi-layer WS_2 flakes can be nano-patterned by electron-beam-lithography (EBL) and subsequent reactive-ion-etching (RIE) [39, 43, 44], making them useful as a material platform for metasurfaces.

In this work, we use an adjoint optimization method [7, 15, 45–47] to create planar chiral metasurfaces made of WS_2. This design technique optimizes the structure by using the gradient of the figure of merit (FOM) with respect to the design parameters through direct and adjoint full-wave simulations. The adjoint optimization enables the realization of a freeform structure that maximizes the FOM while satisfying the design constraints, resulting in a significant performance improvement over conventional heuristic design approaches. The WS_2 chiral metasurface in this work exhibits a high extinction ratio (peak value up to 19.6 dB) in the visible range. Additionally, to verify the performance of the geometric phase manipulation of our designed chiral resonator, we analyze the characteristics of metasurfaces composed of chiral resonators with various rotation angles. These metasurfaces maintain consistently high CDs (>0.5) and transmittance (>0.57) at all rotation angles.

2. Results and discussion

Figure 1(a) illustrates the chiral metasurface and its function, i.e. reflecting a right-hand circularly polarized light (RCP) wave at normal incidence while converting left-hand circularly polarized light (LCP) into an RCP wave in transmission. In this work, WS_2 is chosen for its high refractive index and relatively low absorption in the visible. The WS_2 metasurface is located on a glass substrate with a refractive index of 1.5. Simulations in this work used wavelength-dependent in-plane and out-of-plane refractive indices of WS_2, which are imported from the literature [39]. The relationship between the incident and transmitted circularly polarized light can be written using the Jones matrix calculus in the following form:

$$\begin{pmatrix} E_{tl} \\ E_{tr} \end{pmatrix} = \begin{pmatrix} t_{ll} & e^{-i2\theta} t_{lr} \\ e^{i2\theta} t_{rl} & t_{rr} \end{pmatrix} \begin{pmatrix} E_{il} \\ E_{ir} \end{pmatrix} \tag{1}$$

Here, the subscripts l and r represent LCP and RCP, respectively, while i and t denote incident and transmitted light, respectively. To obtain perfect conversion between RCP and LCP light for realizing metasurface based on the Pancharatnam-Berry phase, the diagonal elements of the matrix, t_{ll} and t_{rr}, should be zero. Assuming the metasurface can minimize these terms, subsequently, the matrix is simplified, yielding two equations: $E_{tl} = e^{-i2\theta} t_{lr} E_{ir}$ and $E_{tr} = e^{i2\theta} t_{rl} E_{il}$, demonstrating the conversion of handedness. To create a metasurface that produces conversion only for LCP, we introduce a design goal of minimizing the conversion of RCP to LCP, i.e. $t_{lr} = 0$.

Each chiral structure exhibits C_2 symmetry as shown in figure 1(b), a constraint we impose for structure optimization. This is because the generated phase modulation covers the full 2π range when the change in geometrical rotation, θ, corresponds to π. A range of different heights of the resonator is tested, and 250 nm demonstrates the highest FOM. In the 3D simulation domain, the structure is pixelated as figure 1(c), where each pixel has a volume of $10 \times 10 \times 10\ \text{nm}^3$. A square lattice array is used with an array periodicity of 380 nm in both the x and y directions.

Figure 2(a) shows the transmission spectra occurring with LCP and RCP illumination of the inverse-designed chiral metasurface. The transmission monitor in this simulation measures the power of the transmitted light and, therefore, does not distinguish the state of polarization. It is noteworthy to mention that the dichroism is significant across a wide range of wavelengths, unlike most previous works where high dichroism is usually limited to a narrow bandwidth [26, 27, 36, 48]. Substantial light intensity contrast is also observed in reflection spectra as shown in figure 2(b) with RCP being reflected more than the LCP. Figure 2(c) shows the absorption spectra under the LCP and RCP incidences. The absorption tends to increase as the wavelength decreases because the absorption coefficient of WS_2 is greater at shorter wavelengths [39]. The absorption of RCP incidence is larger than the absorption of the LCP in the wavelength range of 600–800 nm, which is attributed to the chirality of the metasurface.

Figure 2(d) shows the CD in transmission and reflection and the extinction ratio. The transmission CD is defined as $(T_L – T_R)/(T_L + T_R)$, where T_L and T_R are the transmissions under the LCP and RCP incidences, respectively. Likewise, the reflection CD is defined as $(R_L – R_R)/(R_L + R_R)$. The CD reaches a maximum value of close to unity at $\lambda = 675$ nm

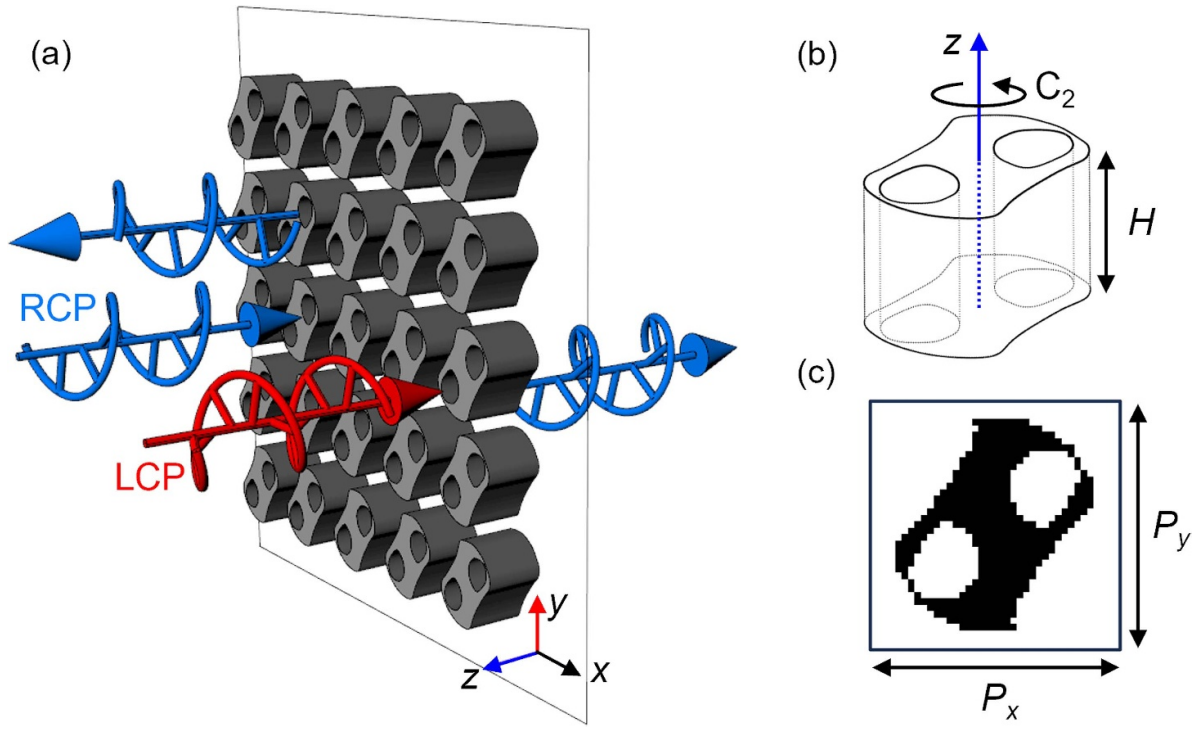

Figure 1. (a) Schematic illustration of the inversely-designed chiral metasurface optimized to reflect right-hand circularly polarized light (RCP, represented with blue colors) while maintaining the polarization and convert left-hand circularly polarized light(LCP, represented with red) to RCP. The metasurface consists of a periodic array of WS_2 chiral resonators on a glass substrate. (b) Illustration of a single WS_2 chiral resonator. The resonator has a two-fold rotational symmetry (C_2) along the z-axis, and the thickness (H) is 250 nm. (c) Top-view of the pixelated chiral resonator in simulations. The black and white pixels represent WS_2 and air, respectively, and the single pixel dimension is $10 \times 10 \times 10\,\text{nm}^3$. The periodicities of an array of the chiral resonators, P_x and P_y, are 380 nm.

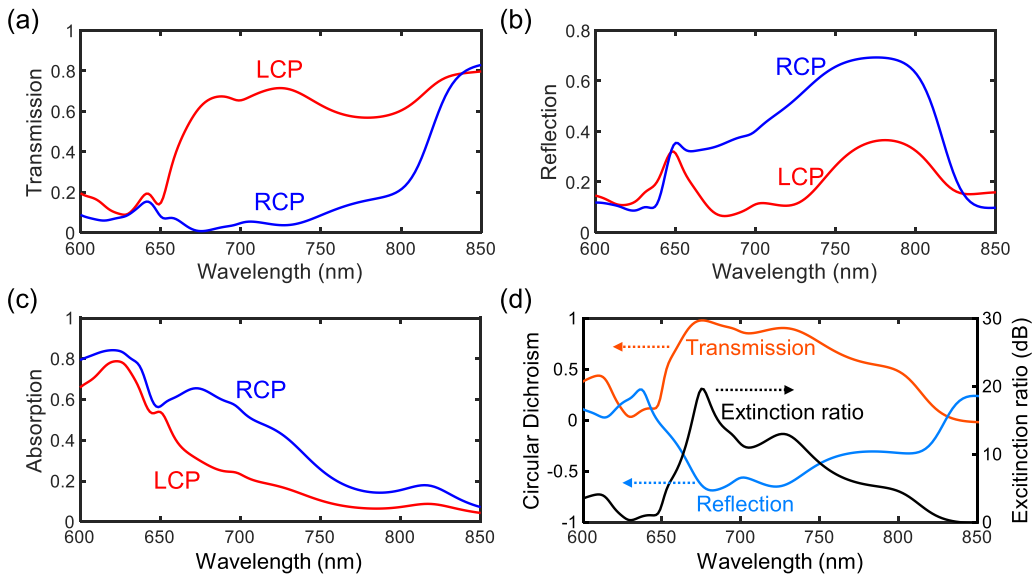

Figure 2. (a) Transmission spectra when LCP (red) and RCP (blue) are incident onto the inversely designed chiral resonator array. (b) Reflection spectra of LCP and RCP incidences. (c) Absorption spectra of LCP and RCP incidences. (d) Circular dichroism in the transmission (orange), reflection (light blue), and extinction ratio (black). The circular dichroism, the difference in light intensity between LCP and RCP, is obtained from the transmission and reflection data in (a) and (b). The extinction ratio, i.e. the ratio of transmittance under RCP and LCP incidence, peaks reaching 19.6 dB at $\lambda = 675$ nm.

and exceeds 0.5 across the spectral window that is $\simeq$147 nm wide. The extinction ratio, which is defined as T_L/T_R, peaks value reaching 19.6 dB at 675 nm. Table 1 demonstrates a comparison of the planar chiral dielectric metasurfaces at various working wavelengths. The table includes information on the material, thickness, absolute CD, extinction ratio, and

Table 1. Comparison of planar chiral dielectric metasurfaces.

Wavelength (μm)	Structure [References]	Material	Thickness (nm)	Transmission	Extinction ratio	Bandwidth[a] (nm)
1.655	Z-shape [26]	Ge	500	≃0.95	≃13.5	≃30
0.997, 1.055	Elliptical cylinders [51]	Si	700	≃0.895, 96.5	≃12.8, 96.5	≃7, 3
1.5	Z-shaped etch [52]	Si	215	≃0.97	≃345	≃74
1.55	Deformed H-shape [53]	Si	452	≃0.96	≃3.8×10^4	≃34
0.545	Gammadion [50]	TiO_2	340	≃0.95	≃31.6	≃13
0.635	Achiral nanofins [49]	Si	450	≃0.65	≃23	≃58
0.675	Layered free-form (this work)	WS_2	250	≃0.67	≃91	≃147

[a] The bandwidth is defined as the wavelength range where |CD| is larger than 0.5.
Note: All data are obtained from the simulation results.

bandwidth of each metasurface. Our proposed metasurface shows the largest bandwidth, which can be attributed to the low Q-factor of the metasurface due to the absorption of WS_2. Furthermore, our metasurface achieves the highest extinction ratio among other metasurfaces operating in the visible range [49, 50].

The very high extinction ratio of the metasurface is enabled by adjoint-optimization-based inverse design with a customized FOM. The FOM ($\mathcal{F}$) of adjoint optimization can be expressed as an inner product between a forward field $\mathbf{E}$ and a target field $\mathbf{E}_d$.

$$\mathcal{F} = \int_{\mathcal{M}} |\mathbf{E}(\mathbf{x}) \cdot \mathbf{E}_d(\mathbf{x})^*|^2 \mathrm{d}A. \tag{2}$$

In our case, $\mathbf{E}_d(\mathbf{x})$ electric field near the metasurface when LCP or RCP light is incident. $\mathbf{E}_d(\mathbf{x})$ is an LCP or RCP plane wave with a constant amplitude that propagates in the $-z$ direction. $\mathcal{M}$ is a monitor plane in the glass substrate and perpendicular to the z-axis, and * indicates a complex conjugate operation. Consequently, $\mathcal{F}$ is directly proportional to the flux of the transmitted LCP or RCP light when the LCP or RCP light is incident. The derivative of $\mathcal{F}$ by the transmitted electric field is

$$\frac{\partial \mathcal{F}}{\partial \mathbf{E}(\mathbf{x})} = \int_{\mathcal{M}} \mathbf{E}_d(\mathbf{x})^* \left[\mathbf{E}(\mathbf{x})^* \cdot \mathbf{E}_d(\mathbf{x})\right] \mathrm{d}A. \tag{3}$$

The variation of the electric field at point $\mathbf{x}$, caused by the adjustment in the permittivity of the design space, can be expressed as

$$\delta\mathbf{E}(\mathbf{x}) = \overleftrightarrow{\mathbf{G}}(\mathbf{x},\mathbf{x}')\mathbf{P}^{\mathrm{ind}}(\mathbf{x}') = \overleftrightarrow{\mathbf{G}}(\mathbf{x},\mathbf{x}')\delta\epsilon(\mathbf{x}')\mathbf{E}(\mathbf{x}'), \tag{4}$$

where $\mathbf{x}$ and $\mathbf{x}'$ indicate the positions in the monitor and the design space, respectively. In addition, $\mathbf{P}^{\mathrm{ind}}(\mathbf{x}')$ indicates the polarization density, which is induced by the variation of the dielectric constant $\delta\epsilon(\mathbf{x}')$, and $\overleftrightarrow{\mathbf{G}}(\mathbf{x},\mathbf{x}')$ is a Green's function which represents the electric field at the point $\mathbf{x}$ generated by the unit dipole at the point $\mathbf{x}'$. The variation of $\mathcal{F}$ is $\delta\mathcal{F} = \frac{\partial\mathcal{F}}{\partial\mathbf{E}}\delta\mathbf{E} + \frac{\partial\mathcal{F}}{\partial\mathbf{E}^*}\delta\mathbf{E}^*$. The adjoint field $\mathbf{E}_{\mathrm{adj}}$ can be expressed as

$$\mathbf{E}_{\mathrm{adj}}(\mathbf{x}') = \int_{\mathcal{M}} \overleftrightarrow{\mathbf{G}}(\mathbf{x},\mathbf{x}') \cdot \left[\mathbf{E}_d(\mathbf{x})^* \left(\mathbf{E}(\mathbf{x})^* \cdot \mathbf{E}_d(\mathbf{x})\right)\right] \mathrm{d}A. \tag{5}$$

The adjoint field can be obtained by setting electric dipoles at the monitor plane with the direction and amplitude of $\mathbf{E}_d^*(\mathbf{E}^* \cdot \mathbf{E}_d)$ because of the Lorentz reciprocity [54]. Finally, the gradient of $\mathcal{F}$ with respect to the permittivity at the point $\mathbf{x}'$ can be expressed as

$$\frac{\partial \mathcal{F}}{\partial \epsilon(\mathbf{x}')} = 2\mathrm{Re}\left[\mathbf{E}(\mathbf{x}') \cdot \mathbf{E}_{\mathrm{adj}}(\mathbf{x}')\right]. \tag{6}$$

To effectively modulate the geometric phase of the transmitted light, $T_{rr} = |t_{rr}|^2$, $T_{lr} = |t_{lr}|^2$, and $T_{ll} = |t_{ll}|^2$ should be minimized. At the same time, $T_{rl} = |t_{rl}|^2$ is required to be maximized, which is the value related to the efficiency of the metasurface. Therefore, we set the total FOM to maximize as a linear combination of partial FOMs, $\mathcal{F}_{rl} - (\mathcal{F}_{rr} + \mathcal{F}_{lr} + \mathcal{F}_{ll})$, where the first and second subscripts of $\mathcal{F}$ refer to the circular polarization of the target field and the incidence in the forward field, respectively. We use open-source finite-differential-time-domain (FDTD) solver MEEP [55] for the forward and backward simulations and MEEP's adjoint module [45] for updating the design parameters. The detailed flow chart of the adjoint optimization is described in the literature [56, 57].

The total simulation space is 380 nm long along the x- and y-directions and 2250 nm high along the z-direction, where the simulation mesh size is 10 nm along the x-, y-, and z-directions. Two perfect matching layers (PMLs), which are 500 nm thick, are positioned at the top ($+z$) and bottom ($-z$) of the simulation space to absorb any outgoing waves. The pairs of the front ($+x$) and back ($-x$) surfaces and the right ($+y$) and left ($-y$) surfaces of the simulation space are set to satisfy periodic Bloch boundary condition to simulate the periodic array

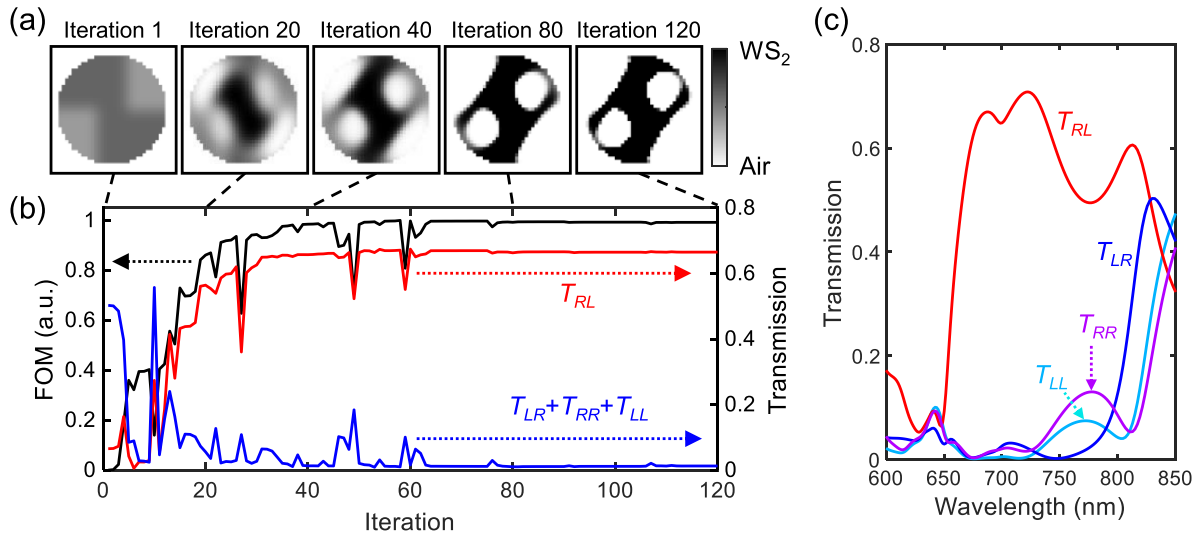

Figure 3. Inverse design procedure for optimizing the WS_2 resonator. (a) The evolution of the design parameters is displayed with the iteration numbers. The colors black and white represent the permittivities of WS_2 and air, respectively, and the grey color indicates permittivity between those of air and WS_2. (b) The evolution of the figure of merit (FOM) and transmission in relation to the number of iterations. T_{RL} and T_{LL} indicate the transmitted light intensity of the RCP (R in subscript) and LCP (L) light when LCP light is incident, respectively. Likewise, T_{RR} and T_{LR} refer to the transmission of the RCP and LCP light when the RCP light is incident. The red line shows T_{RL}, and the blue line represents the sum of three transmissions $T_{LR} + T_{RR} + T_{LL}$ at $\lambda = 680$ nm. (c) The transmission spectra of the chiral resonator array depending on the incident and transmitted polarization, showing extremely small T_{LR}, T_{RR}, and T_{LL} at $\lambda = 680$ nm.

of the resonators. The design space is positioned in the middle of the top and bottom surfaces and is 250 nm high along the z-direction, and the area above and below the design space is filled with air and SiO_2, respectively. The plane wave source is positioned 10 nm below the top PML, and the field monitor and the adjoint source are positioned 10 nm above the bottom PML. The optimization process, which consists of 120 iterations, takes approximately 4 hours using a workstation with a 64-core CPU (Ryzen Threadripper 5995WX). For the final test of the optimized structure, we extend the simulation space to 3250 nm in z-direction to reduce the influence of evanescent waves and insert a reflectance monitor 90 nm below the source plane to measure the reflectance spectra.

We applied additional design constraints and filters for the manufacturable design and effective geometric phase modulation. As shown in figure 3(a), the material outside of the design domain, a circle with 330 nm diameter, is fixed to the permittivity of air to reduce the interaction between neighboring resonators. Furthermore, C_2 symmetry was applied for full phase coverage, e.g. 0 to 2π. Moreover, a subpixel smoothing filter is applied to remove unfabricable fine structures [45]. Binarization weights are used to make the design parameters converge to the permittivities of WS_2 and air [15]. Figure 3(b) shows the evolution of the total FOM and the transmissions with the increasing number of iterations. The FOM rapidly increases until it is saturated in about after the 40th iteration. After saturation, the binarization weights become more dominant than the weights from the gradient of the FOM, pushing design parameters to converge to the permittivity of WS_2 and air. As the FOM increases, T_{RL} increases while T_{RR}, T_{LR}, and T_{LL} decrease. This indicates that the gradient of the FOM effectively enlarges T_{RL} while suppressing the other transmissions. After the 120th iteration, the design parameters are fully binarized to the permittivities of either WS_2 or air. The optimized structure is shown in figure 1 and the appendix. Figure 3(c) shows the transmission spectra of the chiral resonator array depending on the incident and transmitted polarization. T_{RR}, T_{RL}, T_{LL} show extremely low values ($\simeq$0.006) compared to T_{RL} ($\simeq$0.65) at $\lambda = 680$ nm.

Figure 4(a) shows the electric fields under LCP and RCP incidences in xz-plane, and figure 4(b) illustrates the same fields in xy-plane. Both LCP and RCP incidences experience resonant behavior; however, the distribution of the maximum electric field intensities differs with the incident polarization. Under LCP incidence, the lobe is mostly outside the chiral resonator, while it is mostly distributed inside the resonator for RCP incidence, causing comparatively large absorption and low transmission. The notable distinction in the electric field distribution, resulting in the large variation in absorption, may account for the large extinction ratio of the chiral resonator in this work. The optical chiral density [48, 58] distribution is displayed in figure 4(c) to visualize the polarization conversion process induced by the chiral resonator. The optical chiral density is calculated from the equation, $-\frac{\epsilon_0 \omega}{2} \mathrm{Im}(\mathbf{E}^* \cdot \mathbf{B})$, and normalized by its maximum absolute value. Here, ϵ_0 represents the vacuum permittivity, ω is the angular frequency, and $\mathbf{B}$ is the magnetic field. The positive and negative chiral densities indicate left-handed or right-handed chirality, which correspond to the chiralities of LCP and RCP lights, respectively. The magnitude of chiral density presents a chiral intensity, which is directly proportional to the intensity ($\mathbf{E}^* \times \mathbf{B}$) when electric and magnetic fields are orthogonal. Under LCP incidence, positive and negative chiral densities are observed near the resonator, while only the negative chiral

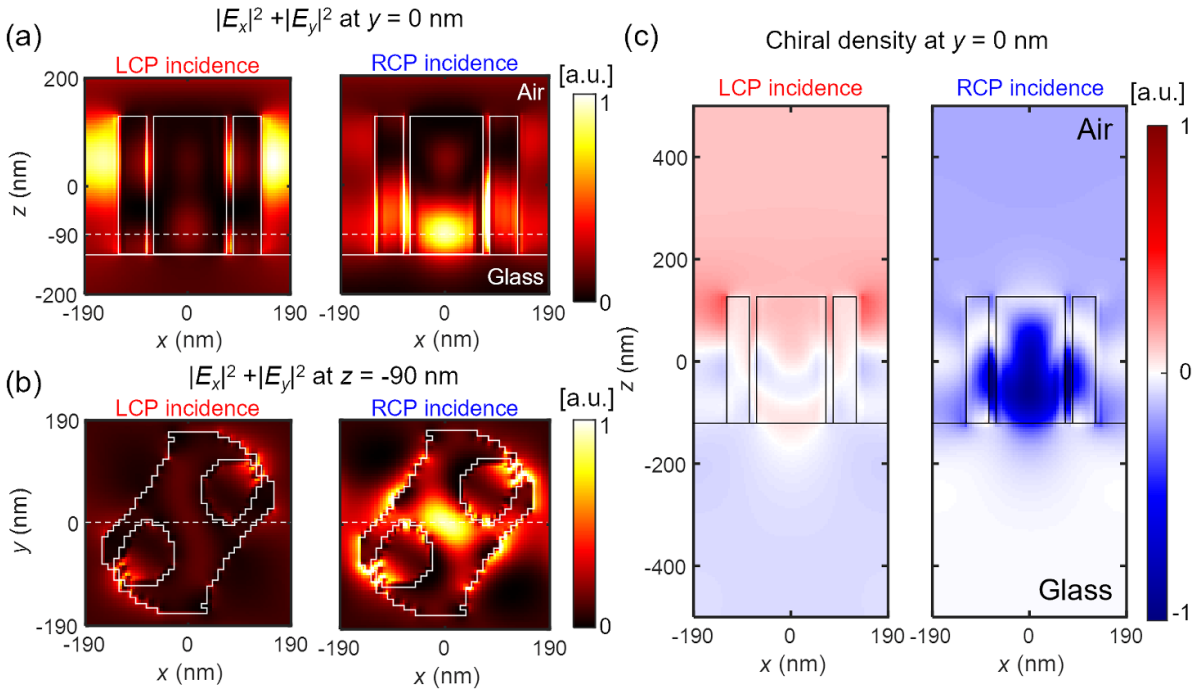

Figure 4. (a) Electric field intensities on the xz-plane under LCP and RCP incidences at $\lambda = 680$ nm. The incident light propagates from top to bottom. Under LCP incidence, the strongest electric field intensity appears outside the WS_2 resonator. On the other hand, under RCP incidence, the strongest electric field appears inside the WS_2 resonator. (b) The electric near field intensities in the xy-plane at $z = -90$ nm under the LCP and RCP incidences at $\lambda = 680$ nm. The RCP incidence creates highly concentrated fields inside the WS_2 resonator, which implicate high absorption compared to the LCP incidence. (c) Optical chiral densities under LCP and RCP incidences. The positive or negative chiral density indicates whether the chirality of LCP or RCP light is dominant at each point, respectively.

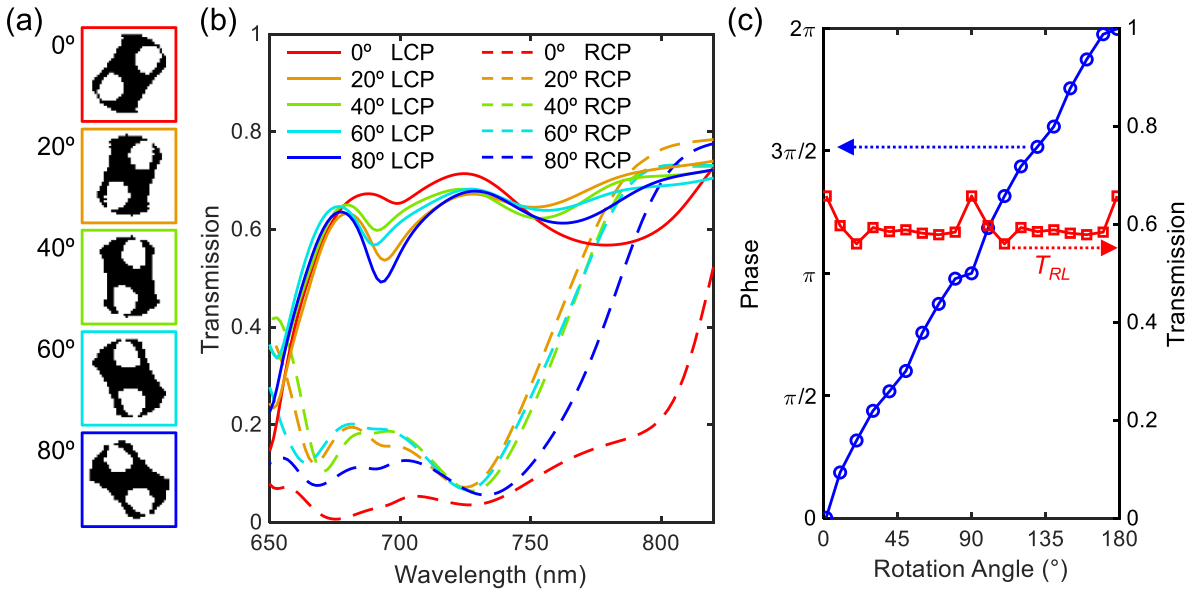

Figure 5. (a) Structures of the chiral resonators with various orientation angles. The structure with rotation angle 0° indicates the non-rotated structure shown in figure 1(c). (b) Transmission spectra for a chiral resonator array with various orientation angles for the LCP (solid lines) and RCP (dashed lines) incidences. The resonator arrays show high circular dichroism with all orientation angles. (c) The transmittance T_{RL} and the relative phases of the RCP light under the LCP incidence in the chiral resonator arrays with various orientation angles at $\lambda = 680$ nm.

density is found at the bottom. This implies that LCP incidence is effectively converted to RCP light by the resonator. In the meantime, under RCP incidence, no red color appears, and the bottom shows white. This indicates that chiral handedness conversion is negligible, and the chirality is not transmitted.

To verify the robustness of the chiral resonator, we tested the optical response with various orientation angles from 0° to 80° as shown in figure 5(a). Figure 5(b) shows transmission spectra of the chiral resonator arrays with varying orientation angles under RCP (dashed lines) and LCP (solid lines) incident light. The transmittance under the RCP incidence increases when the meta-unit is rotated because it changes the coupling between adjacent resonators, resulting in the modification of optical loss [26]. Nevertheless, the resonator arrays still show strong CD across the wide range of wavelengths. Figure 5(c) shows the relative phase of the transmitted RCP light under the LCP incidence (phase of t_{rl}) and transmission T_{RL} at $\lambda =$ 680 nm. The transmission shows a lower bound of 0.56 over the desired bandwidth. Furthermore, the phase almost linearly increases with the rotation angle covering from 0 to 2π. It implies that we can achieve a precise phase modulation using WS_2.

3. Conclusion

In this work, we have demonstrated an inversely designed WS_2 chiral metasurface. We utilized WS_2 as a platform material of the meta-atoms because of its significantly high refractive index and relatively low absorbance at the visible range, which provide great light tunability in an ultrathin layer. We also utilized the inverse design technique based on adjoint optimization to maximize cross-polarized transmission under LCP incidence while blocking RCP incidence. The metasurface exhibits consistently high CD (>0.5) across a wide range of wavelengths (λ of 653–796 nm) and an extremely high extinction ratio (19.6 dB at $\lambda = 675$ nm). Moreover, we have demonstrated geometric phase modulation with the chiral resonator arrays with different orientation angles. They maintained high CD (>0.5) and transmission (>0.56) across all the orientation angles, demonstrating the capability for the geometric phase modulation. Unlike the achiral geometric-phase-based metasurfaces, our chiral metasurface does not require circular polarization filters to reduce the intensity of the light with the unwanted wavefront. Thus, it can realize ultra-compact optics using geometric-phase-based metasurfaces. Furthermore, it may open a new way to advance applications using the chirality of light, such as chiral-sensitive imaging and display technology and platforms of optical spin-orbit interactions.

Data availability statement

The data cannot be made publicly available upon publication because they are not available in a format that is sufficiently accessible or reusable by other researchers. The data that support the findings of this study are available upon reasonable request from the authors.

Acknowledgments

This research was supported by a Grant of the Korea Health Technology R&D Project through the Korea Health Industry Development Institute (KHIDI), funded by the Ministry of Health & Welfare, Republic of Korea (Grant Number: HI19C075300), and also supported by the National Research Foundation of Korea (NRF) Grant funded by the Korean government (MSIT), (NRF-2022K1A3A1A91093776), (RS-2024-00338048), and also supported by the Republic of Korea's MSIT (Ministry of Science and ICT), Under the Global Research Support Program in the Digital Field program (RS-2024-00412644) supervised by the IITP (Institute of Information and Communications Technology Planning & Evaluation), and also supported by Culture, Sports and Tourism R&D Program through the Korea Creative Content Agency Grant funded by the Ministry of Culture, Sports and Tourism in 2024(RS-2024-00332210), and also supported by the artificial intelligence semiconductor support program to nurture the best talents (IITP(2024)-RS-2023-00253914) Grant funded by the Korea government (MSIT), and also supported by the Korea government (MSIT) (RS-2023-00261368). We also acknowledge the Visiting Fellow program at the Department of Electrical and Electronic Engineering, University of Melbourne, for the support hosting J Jo.

Appendix. Optimized metasurface structure

Geometry parameters of the inverse-designed chiral metasurface are displayed in this section. Each value in the array represents a pixel 10 nm wide in the x- and y-direction and 250 nm high along the z-direction. The 38×38 pixels constitute the periodic unit of the metasurface. The value '1' means the pixel is filled with WS_2, while the value '0' means it is filled with air.

00000000000000000000000000000000000000
00000000000000000000000000000000000000
00000000000000000000000000000000000000
00000000000000001111111110000000000000
00000000000000001111111111000000000000
00000000000000001111111111111000000000
00000000000000001111111111111100000000
00000000000000001111111111111111000000
00000000000000001111111110000001000000
00000000000000001111111111000000000100000
00000000000000001111111110000000000100000
00000000000000011111111100000000000010000
00000000000000011111111100000000000011000
00000000000001111111111000000000000111000
00000000000011111111111000000000000111000
00000000001111111111111000000000001111000
00000000001111111111111100000000001111000
00000000011111111111111000000000011110000
00000000111111111111111100000000111100000
00000001111001111111111111001111000000

000000111100000111111111111111110000000
000001111000000011111111111111100000000
000011110000000011111111111111000000000
000011110000000001111111111110000000000
000011100000000001111111111100000000000
000011100000000001111111111000000000000
000011000000000001111111110000000000000
000001000000000001111111110000000000000
000001000000000011111111100000000000000
000001000000000111111111000000000000000
000000100000011111111110000000000000000
000000111111111111111100000000000000000
000000000111111111111100000000000000000
000000000011111111111100000000000000000
000000000000111111111000000000000000000
000000000000011111111100000000000000000
000000000000000000000000000000000000000
000000000000000000000000000000000000000

ORCID iDs

Sangbin Lee https://orcid.org/0009-0009-2563-3764
Sejeong Kim https://orcid.org/0000-0001-9836-3608

References

[1] Malek S C, Overvig A C, Alù A and Yu N 2022 Multifunctional resonant wavefront-shaping meta-optics based on multilayer and multi-perturbation nonlocal metasurfaces *Light Sci. Appl.* **11** 246
[2] Overvig A C, Shrestha S, Malek S C, Lu M, Stein A, Zheng C and Yu N 2019 Dielectric metasurfaces for complete and independent control of the optical amplitude and phase *Light Sci. Appl.* **8** 92
[3] Yu N, Genevet P, Kats M A, Aieta F, Tetienne J-P, Capasso F and Gaburro Z 2011 Light propagation with phase discontinuities: generalized laws of reflection and refraction *Science* **334** 333–7
[4] Jung C, Kim G, Jeong M, Jang J, Dong Z, Badloe T, Yang J K W and Rho J 2021 Metasurface-driven optically variable devices *Chem. Rev.* **121** 13013–50
[5] Wang Y, Yuan Y, Liu Y, Ding X, Ratni B, Wu Q, Nawaz Burokur S, Hu G and Zhang K 2023 Extreme diffraction management in phase-corrected gradient metasurface by Fourier harmonic component engineering *Laser Photon. Rev.* **17** 2300152
[6] Kim J *et al* 2023 Scalable manufacturing of high-index atomic layer–polymer hybrid metasurfaces for metaphotonics in the visible *Nat. Mater.* **22** 474–81
[7] Chung H and Miller O D 2020 High-na achromatic metalenses by inverse design *Opt. Express* **28** 6945–65
[8] Khorasaninejad M, Ting Chen W, Devlin R C, Oh J, Zhu A Y and Capasso F 2016 Metalenses at visible wavelengths: diffraction-limited focusing and subwavelength resolution imaging *Science* **352** 1190–4
[9] Kim J, Yang Y, Badloe T, Kim I, Yoon G and Rho J 2021 Geometric and physical configurations of meta-atoms for advanced metasurface holography *InfoMat* **3** 739–54
[10] Yoon G, Lee D, Tae Nam K T and Rho J 2017 Pragmatic metasurface hologram at visible wavelength: the balance between diffraction efficiency and fabrication compatibility *ACS Photon.* **5** 1643–7
[11] So S, Kim J, Badloe T, Lee C, Yang Y, Kang H and Rho J 2023 Multicolor and 3D holography generated by inverse-designed single-cell metasurfaces *Adv. Mater.* **35** 2208520
[12] Lee G-Y, Hong J-Y, Hwang S, Moon S, Kang H, Jeon S, Kim H, Jeong J-H and Lee B 2018 Metasurface eyepiece for augmented reality *Nat. Commun.* **9** 4562
[13] Wen D, Cadusch J J, Meng J and Crozier K B 2021 Light field on a chip: metasurface-based multicolor holograms *Adv. Photon.* **3** 024001–024001
[14] Ren H, Fang X, Jang J, Bürger J, Rho J and Maier S A 2020 Complex-amplitude metasurface-based orbital angular momentum holography in momentum space *Nat. Nanotechnol.* **15** 948–55
[15] Bae M, Jo J, Lee M, Kang J, Boriskina S V and Chung H 2023 Inverse design and optical vortex manipulation for thin-film absorption enhancement *Nanophotonics* **12** 4239–54
[16] Chen P, Ge S-J, Duan W, Wei B-Y, Cui G-X, Hu W and Lu. Y-Q 2017 Digitalized geometric phases for parallel optical spin and orbital angular momentum encoding *ACS Photon.* **4** 1333–8
[17] White A D, Su L, Shahar D I, Youl Yang K, Ho Ahn G, Skarda J L, Ramachandran S and Vučković J 2022 Inverse design of optical vortex beam emitters *ACS Photon.* **10** 803–7
[18] Pannian Jisha C P, Nolte S and Alberucci A 2021 Geometric phase in optics: from wavefront manipulation to waveguiding *Laser Photon. Rev.* **15** 2100003
[19] Xie X, Pu M, Jin J, Xu M, Guo Y, Li X, Gao P, Ma X and Luo X 2021 Generalized Pancharatnam-Berry phase in rotationally symmetric meta-atoms *Phys. Rev. Lett.* **126** 183902
[20] Yuan Y, Sun S, Chen Y, Zhang K, Ding X, Ratni B, Wu Q, Nawaz Burokur S and Qiu C-W 2020 A fully phase-modulated metasurface as an energy-controllable circular polarization router *Adv. Sci.* **7** 2001437
[21] Basiri A, Chen X, Bai J, Amrollahi P, Carpenter J, Holman Z, Wang C and Yao Y 2019 Nature-inspired chiral metasurfaces for circular polarization detection and full-stokes polarimetric measurements *Light Sci. Appl.* **8** 78
[22] Khorasaninejad M, Chen W T, Zhu A Y, Oh J, Devlin R C, Rousso D and Capasso F 2016 Multispectral chiral imaging with a metalens *Nano Lett.* **16** 4595–600
[23] Chen Y, Yang X and Gao J 2019 3D janus plasmonic helical nanoapertures for polarization-encrypted data storage *Light Sci. Appl.* **8** 45
[24] Li X, Chen L, Li Y, Zhang X, Pu M, Zhao Z, Ma X, Wang Y, Hong M and Luo X 2016 Multicolor 3D meta-holography by broadband plasmonic modulation *Sci. Adv.* **2** e1601102
[25] Yu Bliokh K, Rodríguez-Fortuño F J, Nori F and Zayats A V 2015 Spin–orbit interactions of light *Nat. Photon.* **9** 796–808
[26] Ma Z, Li Y, Li Y, Gong Y, Maier S A and Hong M 2018 All-dielectric planar chiral metasurface with gradient geometric phase *Opt. Express* **26** 6067–78
[27] Semnani B, Flannery J, Al Maruf R and Bajcsy M 2020 Spin-preserving chiral photonic crystal mirror *Light Sci. Appl.* **9** 23
[28] Wang E W, Phan T, Yu S-J, Dhuey S and Fan J A 2022 Dynamic circular birefringence response with fractured geometric phase metasurface systems *Proc. National Academy of Sciences* vol 119 p e2122085119
[29] Naeem T, Kim J, Saad Khaliq H, Seong J, Tariq Saeed Chani M, Tauqeer T, Qasim Mehmood M, Massoud Y and Rho J 2023 Dynamic chiral metasurfaces for broadband phase-gradient holographic displays *Adv. Opt. Mater.* **11** 2202278

[30] Chen Y, Yang X and Gao J 2018 Spin-controlled wavefront shaping with plasmonic chiral geometric metasurfaces *Light Sci. Appl.* **7** 84
[31] Kim S, Lim Y-C, Myeong Kim R, Fröch J E, Tran T N, Tae Nam K and Aharonovich I 2020 A single chiral nanoparticle induced valley polarization enhancement *Small* **16** 2003005
[32] Saad Khaliq H *et al* 2021 Giant chiro-optical responses in multipolar-resonances-based single-layer dielectric metasurfaces *Photon. Res.* **9** 1667–74
[33] Zhang F, Pu M, Li X, Gao P, Ma X, Luo J, Yu H and Luo X 2017 All-dielectric metasurfaces for simultaneous giant circular asymmetric transmission and wavefront shaping based on asymmetric photonic spin–orbit interactions *Adv. Funct. Mater.* **27** 1704295
[34] Ji R *et al* 2021 Chirality-assisted Aharonov–Anandan geometric-phase metasurfaces for spin-decoupled phase modulation *ACS Photon.* **8** 1847–55
[35] Tang B, Li Z, Palacios E, Liu Z, Butun S and Aydin K 2017 Chiral-selective plasmonic metasurface absorbers operating at visible frequencies *IEEE Photonics Technol. Lett.* **29** 295–8
[36] Shi T *et al* 2022 Planar chiral metasurfaces with maximal and tunable chiroptical response driven by bound states in the continuum *Nat. Commun.* **13** 4111
[37] Kim S 2023 All-2D material photonic devices *Nanoscale Adv.* **5** 323–8
[38] Zhang X, Zhang X, Huang W, Wu K, Zhao M, Johnson A T C, Tongay S and Cubukcu E 2020 Ultrathin ws_2-on-glass photonic crystal for self-resonant exciton-polaritonics *Adv. Opt. Mater.* **8** 1901988
[39] Vyshnevyy A A *et al* 2023 van der Waals materials for overcoming fundamental limitations in photonic integrated circuitry *Nano Lett.* **23** 8057–64
[40] Choudhury S M, Wang Di, Chaudhuri K, DeVault C, Kildishev A V, Boltasseva A and Shalaev V M 2018 Material platforms for optical metasurfaces *Nanophotonics* **7** 959–87
[41] Verre R, Baranov D G, Munkhbat B, Cuadra J, Käll M and Shegai T 2019 Transition metal dichalcogenide nanodisks as high-index dielectric mie nanoresonators *Nat. Nanotechnol.* **14** 679–83
[42] Shim H, Monticone F and Miller O D 2021 Fundamental limits to the refractive index of transparent optical materials *Adv. Mater.* **33** 2103946
[43] Munkhbat B, Yankovich A B, Baranov D G, Verre R, Olsson E and Shegai T O 2020 Transition metal dichalcogenide metamaterials with atomic precision *Nat. Commun.* **11** 4604
[44] Kim S, Fröch J E, Christian J, Straw M, Bishop J, Totonjian D, Watanabe K, Taniguchi T, Toth M and Aharonovich I 2018 Photonic crystal cavities from hexagonal boron nitride *Nat. Commun.* **9** 2623
[45] Lin Z, Liu V, Pestourie R and Johnson S G 2019 Topology optimization of freeform large-area metasurfaces *Opt. Express* **27** 15765–75
[46] Nelson D, Kim S and Crozier K B 2023 Inverse design of plasmonic nanotweezers by topology optimization *ACS Photon.* **11** 85–92
[47] Chung H and Miller O D 2020 Tunable metasurface inverse design for 80% switching efficiencies and 144 angular deflection *ACS Photon.* **7** 2236–43
[48] Tang Y and Cohen A E 2010 Optical chirality and its interaction with matter *Phys. Rev. Lett.* **104** 163901
[49] Sarwar Rana A S, Kim I, Afnan Ansari M A, Sabieh Anwar M S, Saleem M, Tauqeer T, Danner A, Zubair M, Mehmood M Q and Rho J 2020 Planar achiral metasurfaces-induced anomalous chiroptical effect of optical spin isolation *ACS Appl. Mater. Interfaces* **12** 48899–909
[50] Zhu A Y, Ting Chen W T, Zaidi A, Huang Y-W, Khorasaninejad M, Sanjeev V, Qiu C-W and Capasso F 2018 Giant intrinsic chiro-optical activity in planar dielectric nanostructures *Light Sci. Appl.* **7** 17158–17158
[51] Ma D, Li Z, Zhang Y, Liu W, Cheng H, Chen S and Tian J 2019 Giant spin-selective asymmetric transmission in multipolar-modulated metasurfaces *Opt. Lett.* **44** 3805–8
[52] Hu J, Zhao X, Lin Y, Zhu A, Zhu X, Guo P, Cao B and Wang C 2017 All-dielectric metasurface circular dichroism waveplate *Sci. Rep.* **7** 41893
[53] Hussain S, Ji R and Wang S 2023 High-performance circular polarization modulation using a dielectric metasurface *Appl. Opt.* **62** 4860–5
[54] Dennis Miller O 2012 *Photonic Design: From Fundamental Solar Cell Physics to Computational Inverse Design* (University of California)
[55] Oskooi A F, Roundy D, Ibanescu M, Bermel P, Joannopoulos J D and Johnson S G 2010 Meep: a flexible free-software package for electromagnetic simulations by the fdtd method *Comput. Phys. Commun.* **181** 687–702
[56] Augenstein Y, Roussey M, Grosjean T, Descrovi E and Rockstuhl C 2022 Inverse design of cavities for bloch surface waves interfaced to integrated waveguides *Photon. Nanostruct. Fundam. Appl.* **52** 101079
[57] Hammond A M, Slaby J B, Probst M J and Ralph S E 2022 Phase-injected topology optimization for scalable and interferometrically robust photonic integrated circuits *ACS Photon.* **10** 808–14
[58] Gryb D, Wendisch F J, Aigner A, Gölz T, Tittl A, Menezes L de S and Maier S A 2023 Two-dimensional chiral metasurfaces obtained by geometrically simple meta-atom rotations *Nano Lett.* **23** 8891–7